Interplay of band occupation, localization, and polaron renormalization for electron transport in molecular crystals: Naphthalene as a case study

Konrad Merkel, Michel Panhans, Sebastian Hutsch, and Frank Ortmann
Department of Chemistry, Technische Universität München, 85748 Garching b. München, Germany

(Received 15 February 2022; revised 29 March 2022; accepted 29 March 2022; published 19 April 2022)

Understanding electronic properties and charge transport in organic semiconductors is important for improving organic electronic materials and devices. Here we investigate the impact of electronic band occupation, charge-carrier concentration, and symmetry of phonon modes on the electron mobility in naphthalene crystals for various temperatures. Our theoretical approach is based on the description of the electron-phonon coupling (EPC), where the coupling to low-frequency modes is treated by an effective vibrational disorder potential with local and nonlocal contributions and the coupling to high-frequency modes is included by a polaron treatment. Surprisingly, the coupling to high-frequency modes leads to an increase in the mobility in presence of the low-frequency modes, which is explained by localization and band occupation effects that further depend on the carrier density. A symmetry analysis sheds additional light on the energy dependence of the EPC, which is important to describe transport properties as a function of charge density and temperature. We also find that coupling to low-frequency phonons together with band occupation effects can lead to a vanishing slope of the mobility versus temperature that is known from experiments.

DOI: 10.1103/PhysRevB.105.165136

I. INTRODUCTION

Over the last decades, organic semiconductors have received increasing attention in fundamental and applied research. The progress in material synthesis, purification techniques and electronic optimization strategies led to a constant improvement of electronic device performance, which makes organic semiconductors very promising candidates for low-cost and easy-to-process electronic and optoelectronic applications [1,2]. This development has resulted in applications such as organic light-emitting diodes [3], organic field-effect transistors [4,5], organic solar cells [6,7], and organic sensors [8], which are now becoming commercially available. Despite the number of applications, there are still great challenges in describing the microscopic charge transport in those materials. Even in the same material such as naphthalene, electrons and holes can behave very differently [9–12] and elude a satisfactory description. While at room temperature the electron mobility along a certain direction is almost temperature-independent, the hole mobility shows a steep power-law behavior [13,14]. A deep understanding of a number of microscopic aspects is essential but has not been achieved yet.

In general, the properties of organic semiconductors depend very sensitively on intra- and intermolecular vibrations. For instance, to understand charge transport it is essential to find a suitable description of the electron-phonon coupling (EPC) that is intrinsic to all organic materials. Within the broad class of organic semiconductors, organic molecular crystals have long-range order, which reduces the complexity as compared to blends or polymers and makes them ideal model systems to study. One important milestone was the development of polaron theories [15–21] that describe the impact of EPC through the formation of a polaron, a charge carrier coherently dressed by dynamic molecular vibrations. This dressing causes a reduction of the electronic bandwidth, also known as band narrowing. This polaronic description is suitable for high-frequency vibrations but questionable for slow (low-frequency) modes [22,23], for which a quasistatic treatment generating electronic disorder was suggested to be more appropriate [22,24]. This disorder and the dynamic change of the same (also referred to as dynamic disorder) is the basis for a description of the transient localization scenario [25–27] at ultrashort time scales. Time-scale analysis become more important in recent research since the molecular vibration spectra are broad and cover two orders of magnitude in energy [28]. A single analytical limit to describe all molecular vibrations, i.e., either dynamic polaron dressing or quasistatic disorder, appears inappropriate and recent models perform a separation into multiple frequency regimes [28–30]. Additionally, numerical methods treating the full dynamics of the molecular vibrations are emerging [31,32].

In this work, we use linear response theory and a dedicated treatment of EPC for low- and high-frequency phonons that combines a vibrational-disorder approach with a polaron approach to calculate electron mobilities in naphthalene crystals. We concentrate on the coupling to only low-frequency phonon modes first and later extend our considerations to all phonon modes. We show that the simultaneous coupling to low- and high-frequency vibrations leads to an unexpected increase of mobility, which is explained in detail. We shed light on temperature dependences of the electron mobility, the role of the charge-carrier density and band-occupation effects, as well as the impact of correlated vibrational disorder across the conduction band.

II. THEORY AND METHODS

A. Holstein-Peierls Hamiltonian

The arrangement of organic molecules in a periodic crystal structure leads to an overlap of molecular orbitals, which enable charge carriers to spread across the crystal. Inter- and particularly intramolecular vibrations in the crystal change the overlap of orbitals and thus directly affect the electronic properties and charge transport, which is called EPC. We model these properties of organic crystals by utilizing the Holstein-Peierls Hamiltonian [17,19],

$$H = H_{\mathrm{el}} + H_{\mathrm{ph}} + H_{\mathrm{el-ph}}. \tag{1}$$

The electronic Hamiltonian is given by an *effective tight-binding* model, where every molecule represents a single site

$$H_{\mathrm{el}} = \sum_{ij} \epsilon_{ij}\, a_i^\dagger a_j, \tag{2}$$

$a_i^{(\dagger)}$ annihilates (creates) an electron at the lowest unoccupied molecular orbital (LUMO) of the ith molecule. Inter- and intramolecular vibrations (phonons) are described by harmonic oscillators

$$H_{\mathrm{ph}} = \sum_{\boldsymbol{Q}} \hbar\omega_{\boldsymbol{Q}} \left(b_{\boldsymbol{Q}}^\dagger b_{\boldsymbol{Q}} + \frac{1}{2} \right), \tag{3}$$

where the index $\boldsymbol{Q} \equiv (\lambda,\ \boldsymbol{q})$ is composed of λ the mode index and $\boldsymbol{q}$ the phonon momentum. The EPC Hamiltonian is given by

$$H_{\mathrm{el-ph}} = \sum_{ij} \sum_{\boldsymbol{Q}} \hbar\omega_{\boldsymbol{Q}} g_{ij}^{\boldsymbol{Q}} (b_{\boldsymbol{Q}}^\dagger + b_{-\boldsymbol{Q}}) a_i^\dagger a_j, \tag{4}$$

where the coupling constant $g_{ij}^{\boldsymbol{Q}}$ can be written as

$$g_{ij}^{\boldsymbol{Q}} = \frac{1}{\sqrt{2N_\Omega \hbar\omega_{\boldsymbol{Q}}^3}} \sum_{n\mu} \boldsymbol{e}_{n\mu}^\lambda(\boldsymbol{q}) \boldsymbol{C}_{ij}^{n\mu}, \tag{5}$$

with polarization vectors

$$\boldsymbol{e}_{n\mu}^\lambda(\boldsymbol{q}) = \boldsymbol{e}_\mu^\lambda(\boldsymbol{q}) e^{i\boldsymbol{q}\boldsymbol{R}_n^0}, \tag{6}$$

and the gradients of the transfer integrals with respect to atomic displacements

$$\boldsymbol{C}_{ij}^{n\mu} = \frac{1}{\sqrt{M_\mu}} \frac{\partial \epsilon_{ij}}{\partial \boldsymbol{R}_{n\mu}} \bigg|_{\boldsymbol{R}_{n\mu} = \boldsymbol{R}_{n\mu}^0}. \tag{7}$$

Here, the index n runs over all unit cells and μ over all atoms inside the unit cell. $\boldsymbol{R}_{n\mu}$ is the position of an atom, $\boldsymbol{R}_{n\mu}^0$ the associated equilibrium position, and M_μ its mass. The vectors $\boldsymbol{C}_{ij}^{n\mu}$ account for changes in the electronic structure due to displacements of atoms and have the full crystal symmetry. Information about phonon mode patterns are contained in the polarization vectors, which are composed of the mode patterns $\boldsymbol{e}_\mu^\lambda(\boldsymbol{q})$, which are the eigenvectors of the dynamical matrix [33], and a phase factor $e^{i\boldsymbol{q}\boldsymbol{R}_n^0}$ due to a finite wave vector $\boldsymbol{q}$.

Unfortunately, the Holstein-Peierls Hamiltonian cannot be solved analytically for large crystals with many phonon modes. Typical problems are the phonon dispersion and the large number of modes, which lead to an exponentially increasing Hilbert space with increasing system size. In the following, we discuss an analytic approach how such obstacles can be approached.

B. Phonon symmetry and phonon dispersion relation

The challenge of describing the $\boldsymbol{q}$ dependence of the EPC is often circumvented by assuming dispersionless optical phonons [34–37,12,18]. However, such a description could leave out essential physics as has been demonstrated for one-dimensional (1D) models of organic molecular crystals [38,39]. Notwithstanding, in 3D bulk crystals the influence of phonons with a nontrivial $\boldsymbol{q}$ dispersion relation is rarely explored but we believe that this would contribute to a better description of charge transport in crystalline organic semiconductors [40].

To interpolate $g_{ij}^{\boldsymbol{Q}}$ throughout the Brillouin zone (BZ), we start with Eq. (5) and restrict the sum over all unit cells n to the unit cells of the involved transfer integral, i.e., the unit cell which contains the sites $\boldsymbol{R}_i$ or $\boldsymbol{R}_j$. For organic molecular crystals, this is a good approximation because of the rapidly decaying orbital overlap, which also entails rapidly decaying couplings with orbital distance. As a result, changes in the geometry outside the involved unit cells do not affect the transfer integral. Performing this approximation allows us to continue analytically and yields

$$g_{ij}^{\boldsymbol{Q}} \approx \frac{1}{\sqrt{2N_\Omega \hbar\omega_\lambda^3}} \sum_\mu \left(\boldsymbol{e}_{n(i)\mu}^\lambda(\boldsymbol{q}) \boldsymbol{C}_{ij}^{n(i)\,\mu} + \boldsymbol{e}_{n(j)\mu}^\lambda(\boldsymbol{q}) \boldsymbol{C}_{ij}^{n(j)\,\mu} \right). \tag{8}$$

The indexes i and j run over all molecules in the crystal and can also be described by their corresponding unit cell index $n(i)$ or $n(j)$ and molecule indexes μ within their unit cell. The vectors $\boldsymbol{e}_{n(i)\mu}^\lambda$ denote the corresponding mode patterns according to unit cell $n(i)$, which is related to the mode pattern in unit cell $n(j)$ by,

$$\boldsymbol{e}_{n(j)\mu}^\lambda = \boldsymbol{e}_{n(i)\mu}^\lambda e^{i\boldsymbol{q}\left(\boldsymbol{R}_{n(j)}^0 - \boldsymbol{R}_{n(i)}^0\right)}, \tag{9}$$

where $\boldsymbol{R}_{n(i)}^0$ is the *position of the unit cell*, in which site i is located. It is not to be confused with the *position of the ith molecule* $\boldsymbol{R}_i$. As a result, the EPC constants are solely determined by the mode patterns inside the unit cell and neighboring unit cells in the crystal lattice, which corresponds to an interpolation of the $\boldsymbol{q}$ dispersion of $g_{ij}^{\boldsymbol{Q}}$ on the basis of two wave functions. A systematic improvement with more terms is straightforward but not in the scope of the present work.

We next define the symmetric (s) and antisymmetric (a) EPC parameters as

$$g_{ij}^{\mathrm{s}\,\lambda}(\boldsymbol{q}) := \frac{1}{\sqrt{2\hbar\omega_\lambda^3(\boldsymbol{q})}} \sum_\mu \boldsymbol{e}_\mu^\lambda(\boldsymbol{q}) \boldsymbol{C}_{ij}^{n_{\mathrm{s}}(i)\,\mu},$$

$$g_{ij}^{\mathrm{a}\,\lambda}(\boldsymbol{q}) := \frac{1}{\sqrt{2\hbar\omega_\lambda^3(\boldsymbol{q})}} \sum_\mu \boldsymbol{e}_\mu^\lambda(\boldsymbol{q}) \boldsymbol{C}_{ij}^{n_{\mathrm{a}}(i)\,\mu}, \tag{10}$$

with the symmetrized and antisymmetrized gradients of the transfer integrals,

$$\begin{aligned} \boldsymbol{C}_{ij}^{n_{\mathrm{s}}(i)\,\mu} &= \boldsymbol{C}_{ij}^{n(i)\,\mu} + \boldsymbol{C}_{ij}^{n(j)\,\mu}, \\ \boldsymbol{C}_{ij}^{n_{\mathrm{a}}(i)\,\mu} &= \boldsymbol{C}_{ij}^{n(i)\,\mu} - \boldsymbol{C}_{ij}^{n(j)\,\mu}, \end{aligned} \tag{11}$$

respectively, and obtain

$$\begin{aligned} g_{ij}^{\boldsymbol{Q}} = &\frac{g_{ij}^{\mathrm{s}\,\lambda}(\boldsymbol{q})}{2\sqrt{N_\Omega}}\left(e^{i\boldsymbol{q}\boldsymbol{R}_{n(i)}^0} + e^{i\boldsymbol{q}\boldsymbol{R}_{n(j)}^0}\right) \\ &+ \frac{g_{ij}^{\mathrm{a}\,\lambda}(\boldsymbol{q})}{2\sqrt{N_\Omega}}\left(e^{i\boldsymbol{q}\boldsymbol{R}_{n(i)}^0} - e^{i\boldsymbol{q}\boldsymbol{R}_{n(j)}^0}\right). \end{aligned} \tag{12}$$

The EPC is hereby (without further approximations) expressed in terms of symmetric and antisymmetric coupling constants and therefore the $\boldsymbol{q}$ dependence of the EPC constant can be split into symmetric and antisymmetric contributions, which turns out to be very useful for later analysis. The EPC constants $g_{ij}^{\mathrm{s(a)}\,\lambda}(\boldsymbol{q})$ themselves are still a function of phonon momentum. From Eq. (12), we see that the symmetric coupling has the strongest impact for $\boldsymbol{q} = 0$ and the weakest for $\boldsymbol{q}$ being at the edge of the BZ. For antisymmetric coupling the behavior is opposite [39]. The symmetric coupling constant $g_{ij}^{\mathrm{s}\,\lambda}(\boldsymbol{q})$ can be evaluated at the BZ center (Γ point) and the antisymmetric coupling constant $g_{ij}^{\mathrm{a}\,\lambda}(\boldsymbol{q})$ at the edge of the BZ. From Eqs. (10) to (12), we can immediately see that the antisymmetric coupling vanishes for $n(i) = n(j)$, i.e., when both molecular sites i and j are located in the same unit cell. That is, inside a unit cell $[n(i) = n(j)]$ the EPC constant has only symmetric contributions.

The symmetrization of the EPC is illustrated schematically in Fig. 1 for the example of two sites i and j. In this figure, the atom index μ is neglected for simplicity in the mode patterns $\boldsymbol{e}_{n(i)}^{\lambda}$ and in the gradients of the transfer integrals $\boldsymbol{C}_{ij}^{n(i)}$ and the projection $\boldsymbol{e}_{n(i)}^{\lambda}\boldsymbol{C}_{ij}^{n(i)} + \boldsymbol{e}_{n(j)}^{\lambda}\boldsymbol{C}_{ij}^{n(j)}$ is proportional to the EPC coupling constant [cf. Eq. (8)]. Figure 1(a) illustrates that the gradients (orange arrows) are in general different, i.e., $\boldsymbol{C}_{ij}^{n(i)} \neq \boldsymbol{C}_{ij}^{n(j)}$. Symmetrization leads to the symmetrized gradients $\boldsymbol{C}_{ij}^{n_{\mathrm{s}}(i)}$ in Fig. 1(b) and the antisymmetric gradients $\boldsymbol{C}_{ij}^{n_{\mathrm{a}}(i)}$ in Fig. 1(c). The sum of $\boldsymbol{C}_{ij}^{n_{\mathrm{a}}(i)}$ and $\boldsymbol{C}_{ij}^{n_{\mathrm{s}}(i)}$ gives the original gradient $\boldsymbol{C}_{ij}^{n(i)}$. Please note that the mode pattern is not symmetrized. The $\boldsymbol{q}$ dependence of the EPC constant can then be expressed in terms of the (anti)symmetric $\boldsymbol{C}_{ij}^{n_{\mathrm{s(a)}}(i)}$ gradients projected onto the mode patterns in the unit cells $n(i)$ and $n(j)$ yielding the $\boldsymbol{q}$ dispersion given in Eqs. (10) and (12).

Further extending Eqs. (8) and (12) to more neighboring unit cells is possible and would lead to additional symmetry flavors besides (anti-)symmetric EPC. However, such an systematic extension is computationally demanding [40], because it involves simulating large supercells to obtain the material parameters. It is not in the scope of the present work and we focus on symmetric and antisymmetric coupling, which is an improvement over previous publications that are exclusively based on Γ-point phonon modes.

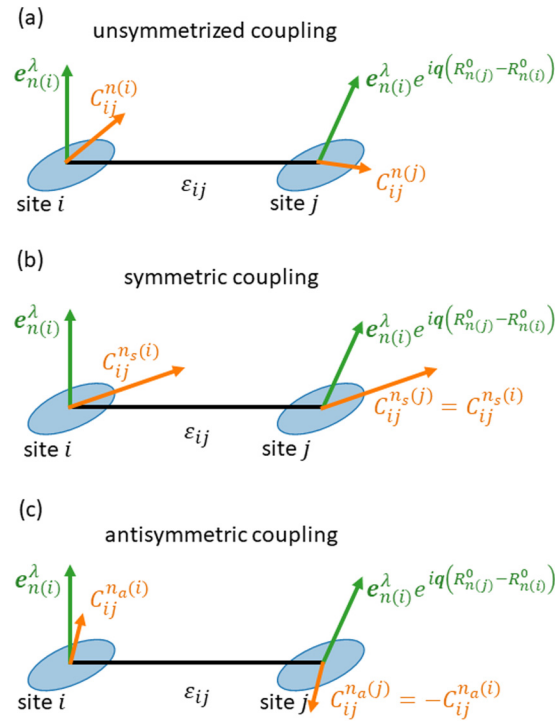

FIG. 1. Schematic view on the relevant contributions to the $\boldsymbol{q}$ dependence of the EPC constants for neighboring molecular sites i and j with transfer integral ε_{ij}. For simplicity, we have dropped the atomic index μ in the mode patterns $\boldsymbol{e}_{n(i)}^{\lambda}$ and $\boldsymbol{e}_{n(j)}^{\lambda}$ and in the gradients $\boldsymbol{C}_{ij}^{n(i)}$ and $\boldsymbol{C}_{ij}^{n(j)}$(see Eq. (7) for their definition). (a) Unsymmetrized gradients used in Eq. (8). (b) Symmetrized gradients $\boldsymbol{C}_{ij}^{n_s(i)}$ as introduced in Eq. (10) to define the $\boldsymbol{q}$ dependence of the symmetric part of the EPC constant $g_{ij}^{s\,\lambda}(\boldsymbol{q})$. (c) Antisymmetrized gradients $\boldsymbol{C}_{ij}^{n_a(i)}$ as introduced in Eq. (10) to define the $\boldsymbol{q}$ dependence of the antisymmetric part of the EPC constant $g_{ij}^{a\,\lambda}(\boldsymbol{q})$.

C. Effective description of electron-phonon coupling

1. EPC to low-energy phonon modes

In our study, we combine the two different theoretical concepts of (adiabatic) quasistatic disorder and polaron narrowing to cover the effect of EPC of different modes with improved accuracy. The first treats the phonon modes within the adiabatic limit of EPC, in which the vibrational mode energies are small compared to the electronic transfer integrals. This leads to an effective description of EPC in terms of dynamic or vibrational disorder for EPC to low-frequency modes. The effectiveness of vibrational disorder treatments has been shown for model systems by previous studies [38,39,41]. They show that not only the high-frequency modes but also the coupling to quasistatic modes are essential to understand the dynamics of charge carriers.

Here, we introduce a real-space formulation of the nonlocal, temperature-dependent vibrational disorder operator $V(T)$ that generalizes local vibrational disorder used previously [42,28]. More details on the derivation of vibrational disorder can be found in the Supplemental Material [43]. We account for the symmetry of the EPC in terms of symmetric and antisymmetric vibrational disorder and

obtain

$$V(T) = V^{\mathrm{s}}(T) + V^{\mathrm{a}}(T), \quad \text{with}$$
$$V^{\mathrm{s(a)}}(T) = \sum_{\lambda ij} \sigma_{ij}^{\mathrm{s(a)}\,\lambda}(T) \frac{\left(\phi_i^\lambda + (-)\phi_j^\lambda\right)}{2} a_i^\dagger a_j, \qquad (13)$$

where ϕ_i^λ are independent, normal-distributed random numbers with zero mean and variance of one. Note that this is a nonlocal disorder potential, which results from the nonlocal EPC. The disorder strengths $\sigma_{ij}^{\mathrm{s(a)}\,\lambda}(T)$ for each mode with its symmetric and antisymmetric coupling parameters are given by

$$\sigma_{ij}^{\mathrm{s(a)}\,\lambda}(T) = g_{ij}^{\mathrm{s(a)}\,\lambda} \hbar\omega_\lambda \sqrt{(1 + 2\langle n_\lambda \rangle_T)}. \qquad (14)$$

Here, $\langle n_\lambda \rangle_T$ denotes the occupation according to the Bose-Einstein distribution function for phonon mode λ at the absolute temperature T. The absolute values of $\sigma_{ij}^{\mathrm{s(a)}\,\lambda}$ denote the standard deviation of the random disorder. According to Eq. (14), $\sigma_{ij}^{\mathrm{s(a)}}$ consists of a temperature-independent and a temperature-dependent contribution. The temperature-independent part originates from quantum mechanical zero-point vibrations of the phonon modes and is the main difference to a classical description [37]. Please note that the random numbers ϕ_i^λ in Eq. (13) only depend on the site index i and mode λ. Consequently, two transfer integrals t_{ij} and t_{ik}, which share the same site, share the same ϕ_i^λ but may differ in the second random number ϕ_j^λ and ϕ_k^λ if $j \neq k$. The partly randomized transfer integrals are therefore not independent but correlated with an autocorrelation A, whereas on-site energies are not correlated. This corresponds to the physical picture, where, e.g., a molecular vibration would lead to a decrease in distance to a neighboring site and therefore increase the distance to another neighbor in opposite direction. The transfer integrals at one site would increase due to a stronger overlap of molecular orbitals and decrease by the same amount in opposite direction. Thus, the vibrational disorder is correlated.

The sign of $\sigma_{ij}^{\mathrm{s(a)}\,\lambda}$ is related to the autocorrelation between neighboring sites. From the hermiticity of the Hamiltonian, it follows directly that $\sigma_{ij}^{\mathrm{s}} = \sigma_{ji}^{\mathrm{s}}$ and $\sigma_{ij}^{\mathrm{a}} = -\sigma_{ji}^{\mathrm{a}}$. The symmetry of a phonon mode manifests with different correlations of neighboring transfer integrals. Total (anti)symmetric modes generate an autocorrelation of $A = +(-)0.5$ for adjacent transfer integrals along a certain crystal-direction. The mixture of symmetric and antisymmetric modes in a real system would lead to smaller values, i.e., between -0.5 and $+0.5$.

2. EPC to high-frequency phonon modes

The appropriate concept to treat phonon modes which vibrate significantly faster than a typical charge-transfer time can be described suitably by using polaron theories [17–21,5]. It is assumed that the polaron is instantaneously formed after the excess electron (or hole) has been created. In other words, the time scales entail a relaxation of the geometry upon charging that is faster than the charge transfer. The polaron description here is based on the Lang-Firsov (LF) transformation [44], which is a unitary transformation of both electron and phonon operators given by the operator

$$S = \sum_{i\boldsymbol{Q}} g_{ii}^{\boldsymbol{Q}} (b_{\boldsymbol{Q}}^\dagger - b_{-\boldsymbol{Q}}) a_i^\dagger a_i. \qquad (15)$$

This transformation is performed for vibration modes with intramolecular EPC only, whereas the modes with finite intermolecular EPC are effectively described using the vibrational disorder potential. This assumption is always justified when the EPC to typical high-energy phonon modes is dominated by the intramolecular coupling constants $g_{ii}^{\boldsymbol{Q}}$. If we use the proposed model for the $\boldsymbol{Q}$ dependence of the EPC constants we find the real-space representation of the operator S,

$$S = \sum_{i\lambda} g_{ii}^{\mathrm{s}\,\lambda} (b_{i,\lambda}^\dagger - b_{i,\lambda}) a_i^\dagger a_i, \qquad (16)$$

which indicates that only the intramolecular couplings at the Γ point contribute. This is reasonable since prototypical high-energy phonon modes only possess an intramolecular EPC constant. The transformed Hamiltonian is then treated by a mean-field approach that substitutes the transformed electronic part by the phonon average [45,20],

$$\tilde{H}_{\mathrm{el}} \to \langle \tilde{H}_{\mathrm{el}} \rangle_{\mathrm{ph}} = \sum_{ij} (\delta_{ij}(\epsilon_{ii} + V_{ii}(T) - \Delta) + (1 - \delta_{ij})\tilde{P}(\epsilon_{ij} + V_{ij}(T))) a_i^\dagger a_j, \qquad (17)$$

where Δ is the polaron shift $\Delta = \sum_\lambda \hbar\omega_\lambda (g_{ii}^{\mathrm{s}\,\lambda})^2$ and $\tilde{P}$ is the polaron renormalization factor

$$\tilde{P} = \exp\left(- \sum_\lambda \left(g_{ii}^{\mathrm{s}\,\lambda}\right)^2 (1 + 2\langle n_\lambda \rangle_T) \right). \qquad (18)$$

Equation (17) therefore considers both the EPC to the low-energy modes by using the vibrational disorder potential $V(T)$ and the EPC to high-energy modes yielding the polaron renormalization factor $\tilde{P}$ for the electronic transfer integrals as well as the polaron shift Δ of the on-site energies. Details on the chosen mode energy which separates the modes according to the two treatments of the EPC are discussed below.

At this point, we note that, for consistency, the LF transformation also transforms the intermolecular part of the EPC and leads to a renormalization of the vibrational disorder that is caused by intermolecular EPC in the same way as for the electronic transfer integrals [cf. second term on the rhs of Eq. (17)]. This is because only electronic operators in the intermolecular EPC are affected by the LF transformation since phonon operators of different vibrational modes commute with each other.

The effective mean-field Hamiltonian in Eq. (17) is used below to evaluate the current-current correlation function for the coherent contributions to charge transport (cf. [45]) with an *ab initio* description of the Hamiltonian parameters. We note that the high-frequency modes do not lead to incoherent transport contributions because they are not thermally activated.

D. Charge transport simulations

We use the framework of linear-response theory by applying the Kubo formula [46–48] for the longitudinal electrical

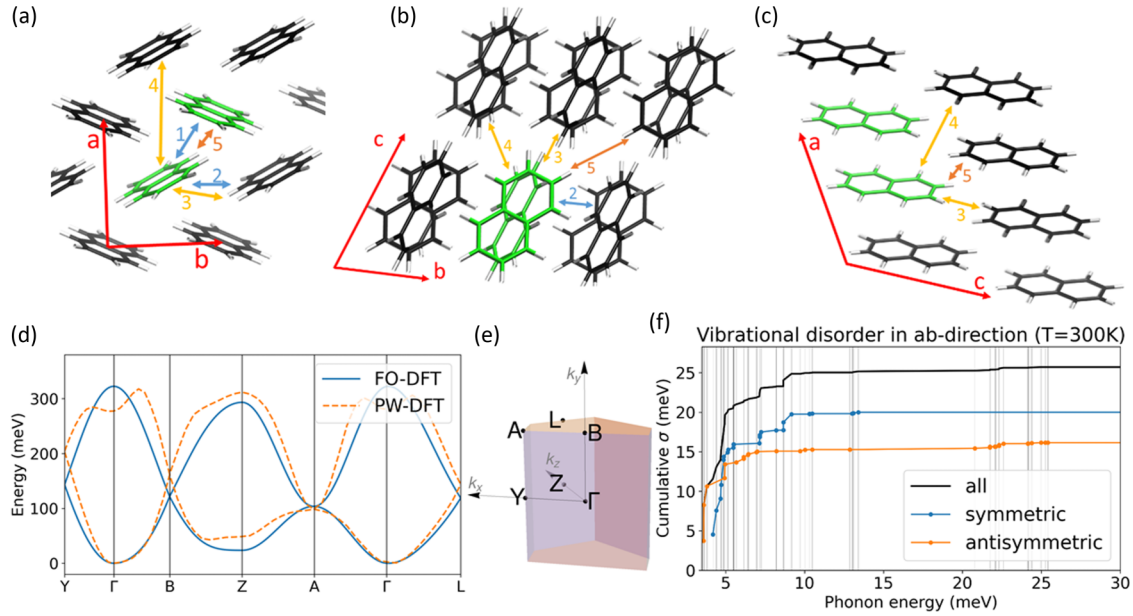

FIG. 2. (a)–(c) Naphthalene crystal and definition of transfer integrals with their ordering number (see Table I). Molecules of a single, primitive unit cell are shown in green. (d) Band structure from fragment-orbital (FO) and plane-wave (PW) DFT simulations. The energy zero is set to the valence band minimum. (e) Half of the Brillouin zone and definition of k points. The used k points in the plot include: Y = (0.5, 0.0, 0.0), Γ = (0.0, 0.0, 0.0), B = (0.0, 0.5, 0.0), Z = (0.0, 0.0, 0.5), A = (0.5, 0.5, 0.0), L = (0.0, 0.5, 0.5). (f) Cumulative variance of the vibrational disorder in the *ab* direction for symmetric (blue) and antisymmetric (orange) EPCs as well as combined σ (black line) plotted against the energy cutoff for quasistatic phonons. Vertical gray lines indicate phonon modes. Every phonon mode is either symmetric or antisymmetric. To show if a phonon mode couples (anti-)symmetrically small blue (orange) dots are used.

conductivity $\sigma_{\alpha\alpha}$ in the form

$$\sigma^{\mathrm{dc}}_{\alpha\alpha} = \frac{1}{\Omega}\int_0^\beta d\lambda \int_0^\infty dt \mathrm{Tr}[\rho\ j_\alpha(t + i\hbar\lambda)\ j_\alpha(0)], \tag{19}$$

where $\rho = e^{-\beta(H-\zeta N)}/Z_{\mathrm{gc}}$ denotes the grand-canonical density operator of the unperturbed system with Hamiltonian H, chemical potential ζ, partition function Z_{gc}, and inverse temperature $\beta = 1/k_B T$. Ω denotes the volume of the crystal and $j_\alpha(t) = e_0 v_\alpha(t)$ is the current operator for the charge carriers, where α is the cartesian component and e_0 the elementary charge.

We evaluate Eq. (19) based on an *ab initio* description of the electronic structure using density-functional theory (DFT) whose details are given further below. Through this connection to DFT, one can treat electron-electron interaction in mean field and continue with effectively noninteracting Kohn-Sham particles for the calculation of the density of states $D(E) = \frac{1}{\Omega}\mathrm{Tr}\{\delta(E-H)\}$ and the energy-resolved mean square displacement

$$\Delta X^2(E,t) = \langle (x(0) - x(t))^2 \rangle_E, \tag{20}$$

with effective single-quasiparticle wave packets [49]. The notation $\langle O \rangle_E := \frac{\mathrm{Tr}\{\delta(E-H)\ O\}}{\mathrm{Tr}\{\delta(E-H)\}}$ for an operator O denotes the corresponding energy-projected averages.

We employ the efficient Lanczos recursion and continued fraction methods [49–51] to tridiagonalize the Hamiltonian. The time evolution of the system is performed by a Chebyshev polynomial expansion of the time evaluation operator [52]. Furthermore, we apply periodic boundary conditions. The initial state is a random phase state, which allows us to calculate traces as expectation values over the random phase state if the sample is large enough [53]. For our study on naphthalene, we find that a supercell consisting of 325 × 416 × 180 primitive unit cells is sufficiently large to calculate numerically converged results.

Finally, the longitudinal mobility is obtained as [49]

$$\mu_{\alpha\alpha}(t) = \frac{\beta e_0}{2n}\frac{d}{dt}\int_{-\infty}^{\infty} dE\ f(E)[1 - f(E)]D(E)\Delta X^2(E,t), \tag{21}$$

where n denotes the charge-carrier density and we have used $\frac{\partial f(E)}{\partial E} = -\beta\ f(E)[1-f(E)]$ with the Fermi function $f(E) = 1/(e^{\beta(E-\zeta)} + 1)$. Equation (21) is used to calculate the time-dependent mobility for a single wave packet propagating coherently in time and space. In a measurement setup, such wave packets could in principle decohere, which we do not model explicitly. The influence of such stochastic decoherence can be captured by introducing an empirical coherence time τ_c, which leads to an exponential decay over time [54],

$$\mu^{\mathrm{dc}}_\alpha = \frac{1}{N}\int_0^{t_{\max}} dt\ e^{-\frac{t}{\tau_c}}\ \mu_\alpha(t), \tag{22}$$

where $N = \int_0^{t_{\max}} dt\ e^{-\frac{t}{\tau_c}}$ is needed for normalization and $t_{\max}$ is the maximum time of our simulation. The coherence time is usually unknown for real systems. However, it needs to be chosen consistently with the energy cutoff for quasistatic modes. A meaningful choice would be $\tau_c = \frac{\hbar}{E_{\mathrm{cut}}}$, where E_{cut} is the energy cutoff for quasistatic phonons.

TABLE I. Transfer integrals for electrons in a naphthalene crystal.

Number	Direction	Symbol	Value [meV]
1	$\pm(\boldsymbol{a}/2 \pm \boldsymbol{b}/2)$	ϵ_{ab}	−37.0
2	$\pm\boldsymbol{b}$	ϵ_{b}	9.9
3	$\pm\boldsymbol{c}$	ϵ_{c}	−3.8
4	$\pm(\boldsymbol{a}+\boldsymbol{c})$	ϵ_{ac}	4.5
5	$\pm(\boldsymbol{a}/2 \pm \boldsymbol{b}/2+\boldsymbol{c})$	ϵ_{abc}	−3.3

III. RESULTS

A. Material parameters for naphthalene

We apply the above theoretical framework to naphthalene as a concrete example. Naphthalene is an organic molecular crystal with two molecules per unit cell arranged in a herringbone-stacking fashion [Figs. 2(a)–2(c)]. We determine all Hamiltonian parameters based on the experimental crystal structure [55,56].

1. Electronic structure

We perform the DFT parametrization of the Hamiltonian for the two lowest conduction bands that are derived from the molecular LUMO states of naphthalene and map them, by representing every LUMO in the crystal by a single site, on an effective tight-binding model, Eq. (2). The transfer integrals between the sites are calculated with the fragment-orbital approach [57–59] using DFT (FO-DFT) and the Gaussian16 code [60] with the basis set 6–311G** [61] and the exchange-correlation-functional B3LYP [62,63]. The obtained transfer integrals are shown in Figs. 2(a)–2(c) with their ordering number used here. The values for all finite transfer integrals are listed in Table I. Only a small number of neighbors have a significant contribution and long-range transfer integrals are exponentially suppressed. The on-site energies ϵ_{ii} can be set to zero.

A straightforward calculation of the band structure from the electronic Hamiltonian Eq. (2) and the transfer integrals in Table I leads to the band energies

$$\begin{aligned}\epsilon(\mathbf{k}) = \epsilon_0 &+ \sum_{i\in\{b,c\}} 2\epsilon_i \cos\mathbf{k}\mathbf{R}_i + 2\epsilon_{ac}\cos\mathbf{k}(\mathbf{a}+\mathbf{c}) \\ &\pm 2\epsilon_{ab}\left(\cos\mathbf{k}\frac{\mathbf{a}+\mathbf{b}}{2} + \cos\mathbf{k}\frac{\mathbf{a}-\mathbf{b}}{2}\right) \pm 2\epsilon_{abc} \\ &\times\left(\cos\mathbf{k}\frac{\mathbf{a}+\mathbf{b}+2\mathbf{c}}{2} + \cos\mathbf{k}\frac{\mathbf{a}-\mathbf{b}+2\mathbf{c}}{2}\right). \quad (23)\end{aligned}$$

Figure 2(d) shows the resulting FO-DFT band structure in blue. As a reference, we have also calculated the band structure with plane-wave DFT (PW-DFT) and B3LYP hybrid functional using the projector augmented-wave method [64,65] of the VASP program package [66,67]. The reference PW-DFT band structure is shown as dashed orange line in Fig. 2(d). The PW-DFT and FO-DFT model agree very well at the bottom of the conduction band, where electron transport takes place. However, differences emerge at higher energies and in the $\boldsymbol{c}$ direction, where distances between molecules are largest. The model is in agreement with previous calculations [68] and for transport properties up to room temperature, such differences should be negligible.

2. Phononic properties and EPC

In the present approach we distinguish between local EPC to the onsite energies of a molecule and the nonlocal EPC to the transfer integrals between two different molecules. In the case of naphthalene, the former predominantly contribute to the polaron renormalization, while local and nonlocal contributions together generate the disorder potential. The local EPC is calculated for an isolated gas-phase molecule using a frozen phonon approach [69] with vibrational patterns and mode frequencies obtained with DFT using Gaussian 16 [60], the basis set 6–311G** [61], and the exchange-correlation-functional B3LYP [62,63].

The nonlocal EPC is calculated with phonon mode patterns and vibration frequencies obtained with the density functional based tight-binding method (DFTB) [70,71]. It has been shown that DFTB yields appropriate estimations of vibrational properties in a computationally efficient way although being less accurate than DFT [72]. We used the DFTB+ program [73] with the 3ob-3-1 parameter set [74,75] for third-order density functional tight binding [76] and included Grimme's dispersion correction [77]. We apply a frozen phonon approach [69], where the atoms in a supercell are displaced according to the phonon mode patterns and changes in ϵ_{ij} (calculated with DFT as explained above) are tracked to obtain $g_{ij}^{\boldsymbol{Q}}$. To sample both the Γ point and BZ edge of the crystal vibrations we have used a supercell with $2\times2\times1$ primitive unit cells (8 molecules).

Antisymmetric modes are located at the BZ edge of the *primitive* unit cell (see the Methods section) and are folded into the BZ center of the *supercell*. Because of the chosen size of the supercell only symmetric and antisymmetric $g_{ij}^{n_{s(a)}\,\lambda}$ are located at the Γ point of the *supercell's* BZ. The distinction between symmetric and antisymmetric modes can be achieved afterwards by checking if $g_{ij}^{\lambda\,\boldsymbol{q}=0}$ is periodic with respect to the *primitive* unit cell (symmetric) or only with respect to the *supercell* (antisymmetric). Finally, we calculate the (anti)symmetric coupling constants $g_{ij}^{s(a)\,\lambda}$ according to Eq. (10) for every phonon mode and the overall vibrational disorder strength $\sigma_{ij}^{s(a)}(T)$ using Eq. (14).

The method of vibrational disorder is strictly valid only if the phonons are static with respect to the electrons dynamics. Therefore only the lowest-energy modes can be treated quasistatically and we need to find a cutoff energy to separate high- and low-frequency modes. Figure 2(f) shows the cumulative vibrational disorder $\sigma_{ij}^{s(a)}(T)$ over different cutoff energies along the largest transfer integral ϵ_{ab} at $T = 300$ K. Vertical lines represent phonon energies. The overall vibrational disorder changes very much for small energy cutoffs and barely changes for higher energies, where more phonon modes are involved.

We performed test simulations for several cutoff energies and compared the electrons dynamics in terms of displacement and localization with the oscillation period of the highest frequency phonon that is treated quasistatically. We found that treating the eight lowest-frequency nonlocal phonon modes with a maximum energy of 4.9 meV as

quasistatic modes yields consistent results, i.e., where the phonon oscillations are quasistatic compared to the electrons dynamics. Similar cutoff energies of 5 meV have been chosen previously for similar organic molecular crystals [41]. In our case the standard deviation $|\sigma_{ij}^{s(a)}|$ of nonlocal vibrational disorder at 300 K is highly anisotropic and reaches from 1.7 meV (38% of ϵ_{ac}) in the *ac* direction to 23.9 meV (241% of ϵ_b) in the *b* direction. The vibrational disorder from local modes is an order of magnitude smaller with a maximum standard deviation of only 0.45 meV.

B. Phonon-mode symmetries and correlation of transfer integrals for quasistatic modes

An important precursor for transport properties is the density of states (DOS). We therefore investigate the influence of the quasistatic phonons and their associated vibrational disorder on the states in the conduction band. Figure 3(a) shows a broadening of the DOS with increasing temperature (increasing vibrational disorder). Higher temperatures lead to an activation of more phonon modes and hence a stronger vibrational disorder. Consequently, the DOS broadens with increasing temperature. Despite the temperature dependence, our data shows that the part of the vibrational disorder [cf. Eq. (14)], which originates from quantum mechanical zero-point vibrations, is significant at all considered temperatures including room temperature. We note that a classical description of EPC, e.g., in the form of a molecular dynamics simulation, would therefore not be able to capture such contributions.

EPC does not homogeneously broaden the DOS but can have a different impact at different energies within the band. To analyze the energy-dependent influence of the EPC on the DOS, we now introduce the energy-resolved absolute coupling constant $G_\lambda^{s(a)}(E)$ of (anti)symmetric modes to establish a measure of the EPC strength projected onto the crystal band energy [38,39] based on the band structure $\epsilon(\boldsymbol{q})$ [cf. Eq. (23)],

$$G_\lambda^{s(a)}(E) = \frac{1}{N_\Omega} \int_{BZ} d^3\boldsymbol{q}\, G_\lambda^{s(a)}(\boldsymbol{q}) \delta(E - \varepsilon(\boldsymbol{q})), \tag{24}$$

with

$$G_\lambda^{s(a)}(\boldsymbol{q}) = \sum_{\langle i,j \rangle} \left| g_{ij}^{s(a)}\, \boldsymbol{Q} \right|^2. \tag{25}$$

The sum includes couplings over all the nearest neighbors that are also connected via a transfer integral.

Figures 3(b) and 3(c) show the impact of the EPC for symmetric and antisymmetric contributions across the band for three different crystal directions (three transfer integrals). In these figures, $G_\lambda^{s(a)}(E)$ is divided by the DOS for better comparison of the couplings. The purely electronic DOS without EPC (gray lines) indicates the energetic position of the electronic band. It is clearly visible that the symmetric coupling is strongest at the band edges, whereas the antisymmetric coupling is dominant in the middle of the band. From Eq. (12) it gets clear that modes with $\boldsymbol{q} = 0$ only couple symmetrically, whereas for $\boldsymbol{q}$ at the edge of the BZ, the antisymmetric coupling is stronger. From the band structure [see Fig. 2(d)] it can be seen that points near the Γ point are related to energies at the band edge and points near the BZ edges are related to energies at the band center. Thus, the symmetry of the coupling (and therefore the autocorrelation of disorder) has a very distinct impact on different energy regions in the band. We note that similar effects were observed in theoretical studies of nonlocal, (anti)symmetric EPC in 1D pentacene chains [39].

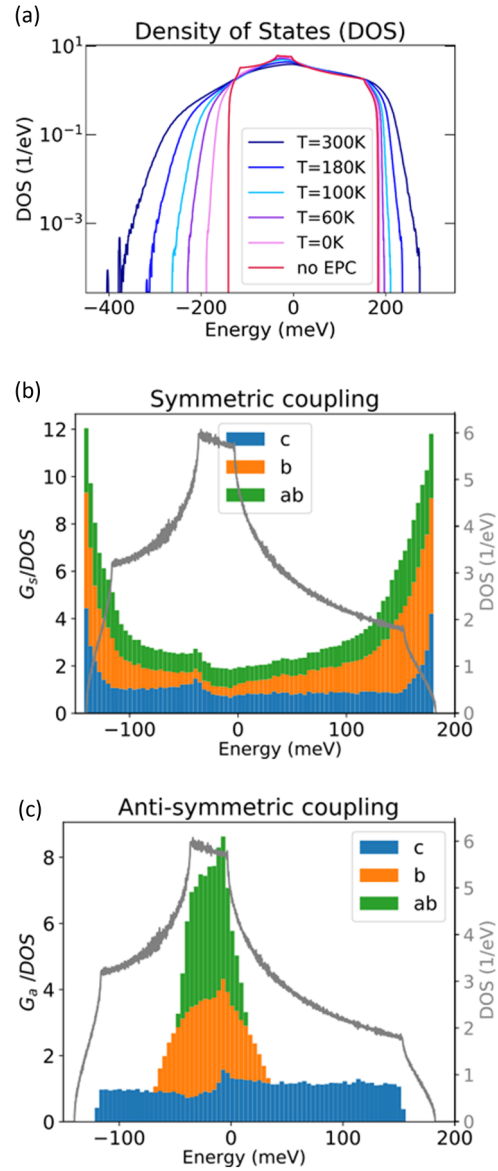

FIG. 3. (a) Temperature dependence of the DOS. Vibrational disorder broadens the DOS even at zero temperatures due to temperature-independent zero-point fluctuations in Eq. (14). For comparison the DOS without any vibrational disorder is shown in red (no EPC). (b), (c) Energy-resolved coupling strength (see Eq. (24) for definition) of purely symmetric EPC (b) and purely antisymmetric EPC (c) for three different directions. DOS without EPC is indicated in gray for clarity.

This observation can be further related to the influence of the couplings at different temperatures and carrier densities. For small temperatures and small charge densities, electrons only populate states near the band edge and therefore symmetric modes dominate EPC. On the other hand, antisymmetric

coupling is more important at higher temperatures and larger charge-carrier densities, because states in the middle of the band become occupied. A detailed analysis of the band occupation is given in the next section.

We next analyze the autocorrelation of the vibrational disorder. The combined vibrational disorder from all phonon modes is correlated with an autocorrelation between the neighboring transfer integrals along a given direction that ranges from $A = 0.1$ (b direction) up to $A = 0.3$ (abc direction). This indicates that both symmetric and antisymmetric modes contribute substantially but symmetric modes are more dominant for every transfer integral. Previous studies of pentacene crystals also have shown a dominance of symmetric coupling with an autocorrelation of 0.25 [22], which agrees with our results on naphthalene.

C. Influence of quasistatic phonon modes on 3D electronic transport in naphthalene crystals

Before we address the influence of EPC on charge transport in all its complexity, we want to investigate the influence of band occupation on transport first. We focus on the case of quasistatic modes only and generalize our findings later systematically to the whole phonon spectrum. We start with the observation that in our model we identify two underlying temperature dependences. One is related to the ensemble of phonons and affects vibrational disorder (see previous section) while the other is bound to the ensemble of electrons, which determines the band occupation and transport energies.

1. Transport level and band occupation

According to the Kubo-Formula in Eq. (21), the mobility depends on the density of transport states defined by $f(E)[1-f(E)]D(E)$, which is to be distinguished from the occupied density of states $f(E)D(E)$. Figure 4 shows the energetic distribution of transport states (colored bold lines) for two temperatures and different charge-carrier densities. Colored areas show the occupation of the band, which differs from the distribution of transport states especially at the band edge. The distribution gets very narrow for low temperatures [Fig. 4(a)] as its full-width-at-half-maximum is proportional to $4k_BT$. For high temperatures [Fig. 4(b)] the distribution gets broader and energy regions close to the band center contribute more to the overall mobility. In general, those states in the middle of the band are more delocalized and a broader distribution would therefore increase the overall mobility if the DOS would remain unchanged.

It becomes clear that the underlying temperature dependences for phonons and electrons have opposite effects on the charge transport. How these temperature dependences influence the mobility will be the subject of discussions in the next sections. We start with the time-dependent mobility of a single electronic wave packet, which than leads to the dc mobility $\mu_\alpha^{\mathrm{dc}}(T)$ in Sec. III C 3.

2. Time-dependent mobility

To calculate transport properties, we use the approach described above (Sec. II D), the calculated DOS, and $\Delta X^2(E,t)$ according to Eq. (20).

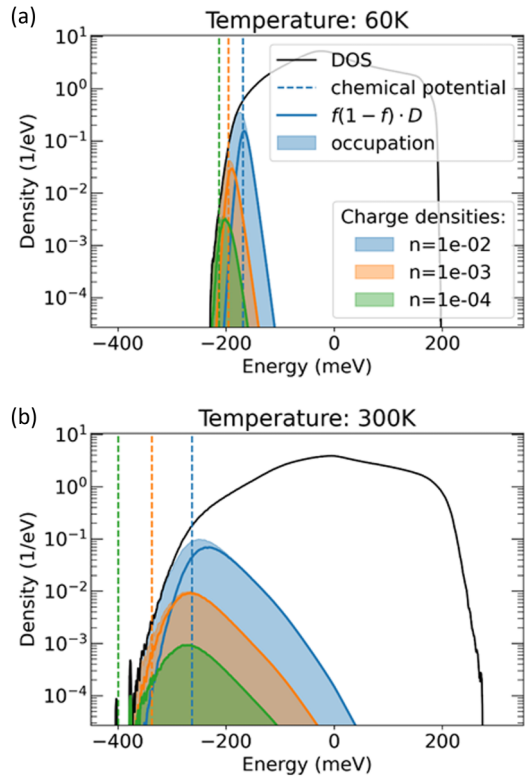

FIG. 4. Occupied density of states (colored areas) and associated density of transport states $\propto f(E)[1-f(E)]D(E)$ (solid lines) for three different charge densities at 60 K (a) and 300 K (b). (a) and (b) use the same legend.

Figure 5 shows the mobility over time in the b direction for three different charge-carrier densities. The vibrational disorder and therefore DOS and $\Delta X^2(E,t)$ are independent of the density. All figures show a typical time dependence. At the shortest times, electrons start spreading across the crystal ballistically (linear increase of mobility up to ∼10 fs, see insets) and eventually get scattered by local and nonlocal vibrational disorder, which leads to destructive interference. Consequently, the mobility decreases and transport becomes diffusive. We find that for a 3D naphthalene crystal vibrational disorder does not lead to a complete localization of electrons.

In Fig. 5(a) we observe that small charge-carrier densities show a sharper and more pronounced initial mobility peak compared to larger densities [cf. Fig. 5(c)]. Small carrier densities lead to transport levels near the band edge. With increasing carrier densities, we observe in Fig. 4 that the density of transport states does not increase as strongly as the density n itself that appears in the $1/n$ prefactor. This leads to a reduced mobility-peak height for larger density, i.e., a lower mobility at short times. For longer times, localization effects set in and lead to a mobility decay. The stronger these effects the sharper is the mobility peak. Consequently, the mobility has a more pronounced peak for small charge densities. A small temperature amplifies this effect, because a smaller energy range is thermally active and higher energy states do not contribute.

At the initial peak, $\mu(t)$ is larger for small temperatures than for larger temperatures. However, for longer times the

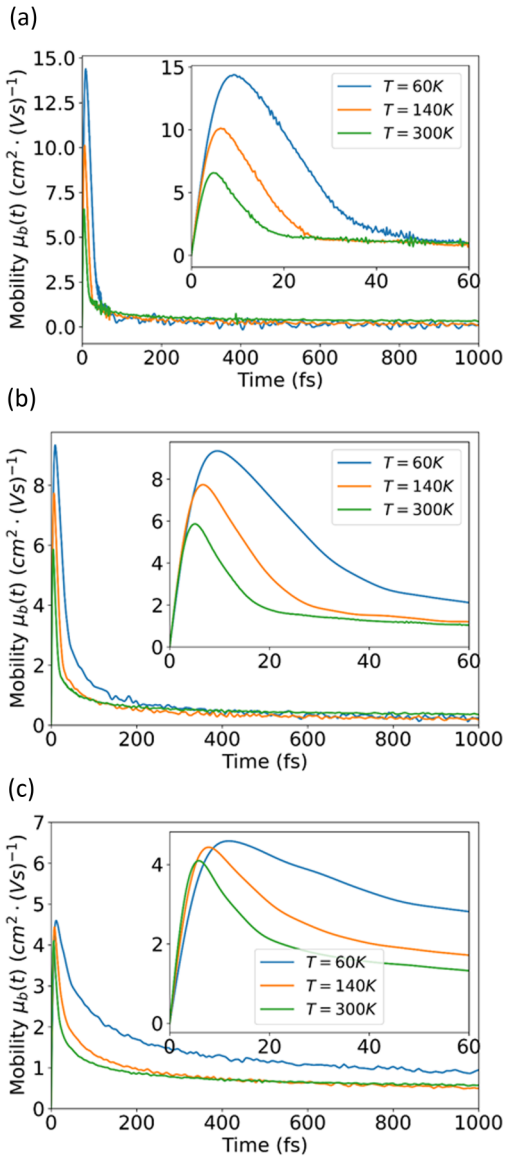

FIG. 5. Time dependent mobility in b-direction for three different charge-carrier densities and temperatures. Charge-carrier density is set to (a) 10^{-4}, (b) 10^{-3} and (c) 10^{-2}. Insets show behaviors at ultrashort times.

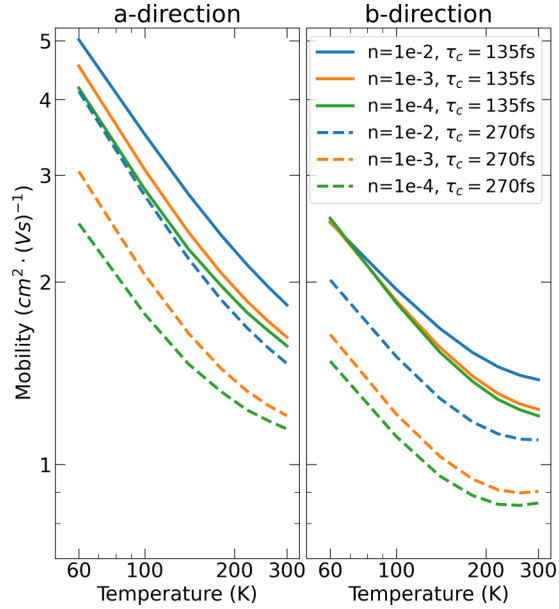

FIG. 6. Temperature-dependent dc mobility for two directions in the herringbone plane. Vibrational disorder stems from the eight lowest quasistatic phonon modes (see main text). Solid lines show the dc mobility for a coherence time of 135 fs, which is consistent with the phonon cutoff energy. Dashed lines indicate a higher coherence time of 270 fs. Colors indicate different charge-carrier densities. The legend applies to both panels.

order is reversed and the mobility at 300 K becomes larger than in the case of 60 or 140 K. This is related to the stronger delocalization of states in the middle of the band, which eventually dominate over the more localized states at the band edge. As discussed in Sec. III B, symmetric coupling has the strongest impact at the band edge while antisymmetric coupling dominates the band center. From this we can conclude that symmetric modes influence the ballistic regime and the initial mobility peak stronger than antisymmetric modes do.

It becomes clear that at different times different energy regions in the conduction band dominate transport. Therefore it depends on the coherence time τ_c how much weight the initial mobility peak gets and how strong the influence of the long-time behavior is. The energy regions of transport are thus influenced by τ_c.

3. Coherence time and dc mobility

Figure 6 shows the dc mobility $\mu_\alpha^{\mathrm{dc}}(T)$ in the herringbone plane according to Eq. (22) for $\tau_c = 135$ fs that is chosen in consistency with the energy cutoff for vibrational disorder and for $\tau_c = 270$ fs which, for comparison, allows for a possibly larger coherence time. Regardless of this choice, the mobility decreases with temperature and shows power law behavior below 150 K. We further analyze the phononic and electronic contributions to the temperature dependency, which affect the mobility additional to the $\beta \propto \frac{1}{T}$ prefactor in Eq. (21). At low T the broadening of the DOS due to EPC and the broader density of transport states are significant and therefore phononic and electronic temperature dependences both codetermine the slope of the power law in Fig. 6. We find that the peak of $\mu_\alpha(t)$ (see Fig. 5) dominates the dc mobility. Therefore the stronger initial mobility peak at lower T leads also to higher mobilities at low T in Fig. 6 and the mobility decreases with increasing temperatures up to 150 K.

At high temperatures, the behavior of μ_α^{dc} in Fig. 6 changes and the slope of the mobility flattens and even suggests the emergence of a high-temperature plateau in the b direction above 200 K. The phonon-induced changes in the DOS are much less pronounced at higher temperatures for the relevant energies around the chemical potential. This is in contrast to low temperatures where the shape of the DOS changes significantly, especially near the chemical potential. However, the broadening of the density of transport states still increases significantly leading to an increased contribution of delocalized states. Thus, the main temperature dependence originates from the thermal occupation of electronic states and not from the temperature-dependent broadening due to vibrational dis-

order. The high-temperature change in the mobility slope (i.e., $\frac{d\mu_\alpha^{\mathrm{dc}}(T)}{dT}$) in Fig. 6 is therefore identified as an effect of band occupation (at constant carrier density).

Figure 6 additionally shows μ_α^{dc} for a larger coherence time. Larger coherence times represent a case in which a charge carrier has more time to localize (see Fig. 5) and the differences between localized and delocalized states appear more strongly. The localization leads to a lower overall mobility and the relevance of the small amount of delocalized states for the mobility increases slightly. Figure 6 shows an emphasized high-T plateau behavior for larger coherence time ($\tau_c = 270$ fs). This indicates that the high-T plateau is mainly driven by the influence of delocalized states in the diffusive transport regime, which, in the middle of the conduction band, are increasingly accessible upon thermal occupation. Additionally, the high-T plateau is more pronounced at higher charge densities. Both observations support the reasoning that the high-temperature plateau is an effect of band occupation.

We want to note that decoherence is a complex phenomenon, where all kinds of external and internal processes, which are not part of the model, can contribute. Any assumed value for the coherence time can therefore only be understood as a simplification, where the whole complexity is reduced to a single parameter. For this reason, we have considered a possible variation of such a number. In general, the coherence time could also be temperature-dependent and would probably decrease with temperature. However, such models are beyond the scope of the present work.

Experimental data on naphthalene electron transport [14,78] show also a power-law behavior for small temperatures and high-temperature plateaus in the b and c directions. In the herringbone-plane (a and b direction) our results coincide qualitatively. However, the simulations cannot describe the out-of-plane direction c. One reason might be that the c direction shows the smallest transfer integrals and therefore possibly has the largest numerical error. More likely, however, we believe the reason lies in the fact that our approach does not contain any inelastic phonon creation or annihilation processes, which might be necessary and have been conjectured in literature [20].

D. Simultaneous modeling of EPC to high-frequency and quasistatic phonon modes

So far, we have discussed EPC due to low-frequency phonon modes only. Now, we want to include the high-frequency modes in a combined model. Below, we discuss the phonon mode spectrum and the associated polaron renormalization, which is used in Sec. III D 2 to calculate the mobility in the presence of low- and high-frequency phonons.

1. Polaron-renormalization and coupling to high-frequency phonon modes

From the EPC parameters $g_{ij}^{\mathrm{s(a)}\,\lambda}$, we obtain the polaron renormalization for high-frequency local phonon modes by applying Eq. (18). We consider all phonons as high-frequency modes whose phonon energy is above a certain threshold. Figure 7 shows the cumulative polaron renormalization of the transfer integrals for different threshold energies over the whole spectrum and for two temperatures. High threshold energies mean only a few modes are considered, whereas low thresholds correspond to situations, where almost all phonons are treated as high-frequency modes. Figure 7 shows that for threshold energies above 70 meV no significant temperature dependence exists, because those modes are not thermally active for either temperatures and only contribute via their quantum mechanical zero-point fluctuations. For threshold energies below 70 meV the occupation of phonon modes (thermal activation) becomes significant and a difference between high and low temperatures is clearly visible.

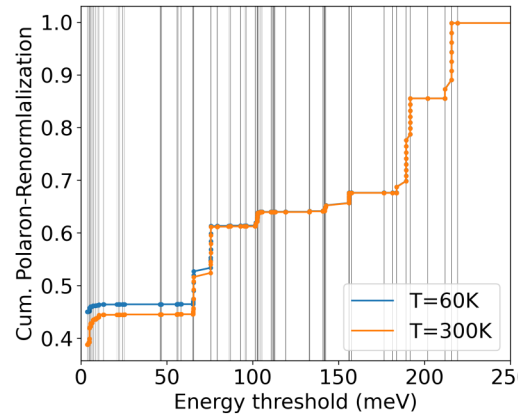

FIG. 7. Polaron renormalization of transfer integrals due to local phonon modes that are above an energy cutoff (abscissa). The cumulated plot indicates no renormalization on the right and increasingly stronger renormalization from right to left due to an increased number of involved modes. Vertical gray lines indicate phonon energies.

In the subsequent transport calculation we treat all quasistatic modes below 4.9 meV with the method of vibrational disorder as before. Higher-frequency modes are treated by polaron renormalization. For this cutoff energy, the polaron renormalization becomes temperature dependent. The corresponding renormalization factor varies from $P = 0.453$ at 60 K to $P = 0.399$ at 300 K.

2. Transport properties

Figure 8 shows the temperature-dependent mobility in the herringbone plane for coupling to high- and low-frequency modes (solid lines), which are compared to simulations with only low-frequency modes from above (dashed lines). We can see that the coupling to high-frequency modes counteracts the formation of the high-temperature plateau at elevated temperatures, but does not add new characteristic features. Surprisingly, polaron renormalization causes an increase of the mobility for all temperatures. Usually, one would expect the opposite since polaron renormalization reduces the transfer integrals, which is expected to impede transport.

A detailed analysis of the DOS in the presence of phononic renormalization shows a narrowing of the band according to Eq. (18) in Fig. 9. The narrowing of the band counteracts the band broadening from vibrational disorder. We can see that the energy rescales but the Fermi-Dirac distribution, which determines the band occupation and density of transport states, remains broad. Only the chemical potential changes to ensure the same charge-carrier density for every simulation. This

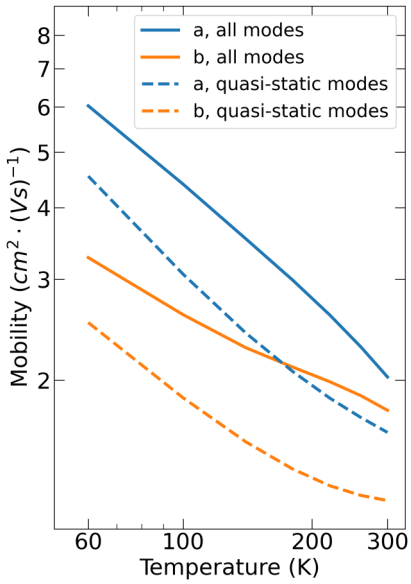

FIG. 8. Combined effects of vibrational disorder and polaron renormalization on electron mobility (solid lines) compared to the case of absence of renormalization (dashed lines). Phonon modes with energies below $E_{\text{cut}} = 4.9$ meV are treated as vibrational disorder. Coherence time is consistent with energy cutoff for quasistatic modes at 135 fs. Charge density is constant at 10^{-3}.

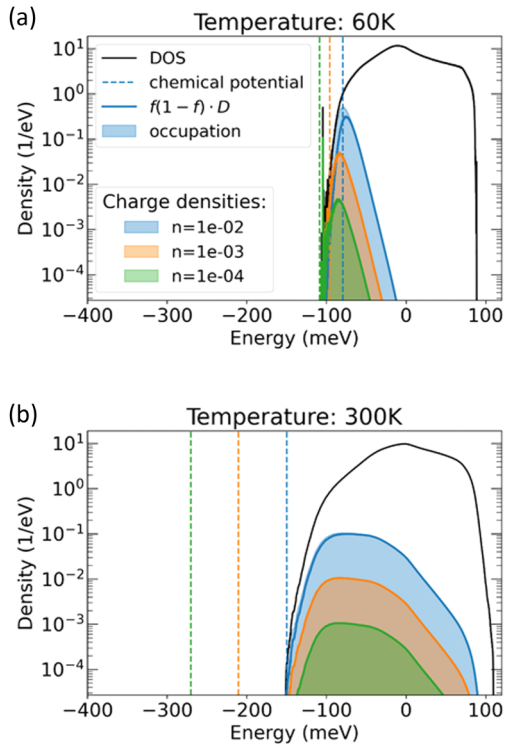

FIG. 9. Occupation of density of states (colored areas) and associated density of transport states $\propto f(E)[1-f(E)]D(E)$ (solid lines) for three different charge densities at 60 K (a) and 300 K (b). (a) and (b) use the same legend. Polaron renormalization leads to band narrowing, which enables the occupation of delocalized states in the middle of the band.

leads to an occupation of states in the middle of the band, which did not contribute before. States in the middle of the band are more delocalized and by occupying those states the effect of the renormalization of the transfer integrals can be overcompensated, which leads to higher mobilities. We want to emphasize that this is a feature of the band structure of naphthalene. Whether polaron renormalization has generally a positive or negative impact on the overall mobility depends on the relative increase of delocalization towards the middle of the band. Microscopic investigations by Vukmirović *et al.* [23] suggest that polaron-renormalization has only a small influence on transport, while we find a factor below two for the present case that is not negligible.

Finally we note that the high-temperature plateau seen in the experiment and our simulations, cannot be associated to polaron renormalization because we observe a stronger decrease of mobility at high temperatures, which counteracts the plateau formation. In any event, our results stress again the importance of EPC to low-frequency modes and the role of band occupation.

IV. CONCLUSIONS

In this paper, we have presented an efficient way to calculate transport properties of a 3D organic molecular crystal in the presence of EPC based on a tight-binding-like representation of the DFT electronic structure and a thoughtful evaluation of the Kubo formula for the electrical conductivity. By splitting the phonon spectrum into quasistatic and dynamical modes, we were able to find effective descriptions in terms of vibrational disorder for low-frequency modes and polaron-renormalization for high-frequency modes. We have shown that not only the variance of vibrational disorder is important, but also the symmetries of the phonon modes. Depending on the symmetry, different regions of the conduction band are affected by EPC to low-frequency phonons, which contribute to charge transport depending on the band occupation.

An in-depth analysis of electron transport in naphthalene has shown the importance of band occupation effects and the role of charge-carrier density. The overall temperature dependency of transport properties originates from the thermal occupation of electronic states, the temperature-dependent broadening of the DOS (due to vibrational disorder), and polaron renormalization when EPC to high-frequency phonons is considered. We found that the experimentally observed high-temperature flattening in the *b* direction can be caused by band occupation and the coupling to low-frequency phonons even when inelastic phonon creation and annihilation processes are not included.

Finally, we investigated the combined effects of EPC to high- and low-frequency modes simultaneously and found the interesting result that the mobility increases by including the interaction to high-frequency modes, i.e., formation of polarons. This counterintuitive finding could be explained as the combined effect of band narrowing and vibrational disorder, which leads to an occupation of delocalized states in the middle of the band that would not contribute otherwise. The occupation effect overcompensates the decrease of transfer integrals between molecular sites due to polaron renormalization.

ACKNOWLEDGMENTS

We thank the Deutsche Forschungsgemeinschaft for financial support [CRC 1415 and projects No. OR 349/1 and No. OR 349/3 and the Cluster of Excellence e-conversion (Grant No. EXC2089)]. Grants for computer time from the Zentrum für Informationsdienste und Hochleistungsrechnen of TU Dresden and the Leibniz Supercomputing Centre in Garching are gratefully acknowledged.

[1] M. E. Gershenson, V. Podzorov, and A. F. Morpurgo, Rev. Mod. Phys. **78**, 973 (2006).

[2] O. Ostroverkhova, Chem. Rev. **116**, 13279 (2016).

[3] S. Reineke, M. Thomschke, B. Lüssem, and K. Leo, Rev. Mod. Phys. **85**, 1245 (2013).

[4] Y. Yuan, G. Giri, A. L. Ayzner, A. P. Zoombelt, S. C. B. Mannsfeld, J. Chen, D. Nordlund, M. F. Toney, J. Huang, and Z. Bao, Nat. Commun. **5**, 3005 (2014).

[5] A. L. Briseno, S. C. B. Mannsfeld, M. M. Ling, S. Liu, R. J. Tseng, C. Reese, M. E. Roberts, Y. Yang, F. Wudl, and Z. Bao, Nature (London) **444**, 913 (2006).

[6] A. J. Gillett, A. Privitera, R. Dilmurat, A. Karki, D. Qian, A. Pershin, G. Londi, W. K. Myers, J. Lee, J. Yuan *et al.*, Nature (London) **597**, 666 (2021).

[7] M. K. Riede, R. Schueppel, K. Schulze, D. Wynands, R. Timmreck, C. Uhrich, A. Petrich, M. Pfeiffer, E. Brier, E. Reinold *et al.*, in *Photonics for Solar Energy Systems II*, edited by A. Gombert (SPIE, New York, 2008), p. 70020G.

[8] S. Xing, V. C. Nikolis, J. Kublitski, E. Guo, X. Jia, Y. Wang, D. Spoltore, K. Vandewal, H. Kleemann, J. Benduhn *et al.*, Adv. Mater. **33**, 2102967 (2021).

[9] N. Karl, in *Organic Semiconductors (Landolt-Börnstein Numerical Data and Functional Relationships in Science and Technology (New Series), Group III)*, edited by O. Madelung, M. Schulz, and H. Weiss (Springer, Berlin, 1985), Vol. 17i.

[10] N.-E. Lee, J.-J. Zhou, L. A. Agapito, and M. Bernardi, Phys. Rev. B **97**, 115203 (2018).

[11] F. Ortmann, F. Bechstedt, and K. Hannewald, New J. Phys. **12**, 023011 (2010).

[12] K. Hannewald and P. A. Bobbert, Appl. Phys. Lett. **85**, 1535 (2004).

[13] N. Karl, K.-H. Kraft, J. Marktanner, M. Münch, F. Schatz, R. Stehle, and H.-M. Uhde, J. Vac. Sci. Technol. A **17**, 2318 (1999).

[14] N. Karl, Synth. Met. **133–134**, 649 (2003).

[15] S. I. Pekar, Zh. Eksp. Teor. Fiz **16**, 335 (1946).

[16] S. I. Pekar, J. Phys. USSR **10**, 341 (1946).

[17] T. Holstein, Ann. Phys. **8**, 343 (1959).

[18] K. Hannewald and P. A. Bobbert, Phys. Rev. B **69**, 075212 (2004).

[19] K. Hannewald, V. M. Stojanović, J. M. T. Schellekens, P. A. Bobbert, G. Kresse, and J. Hafner, Phys. Rev. B **69**, 075211 (2004).

[20] F. Ortmann, F. Bechstedt, and K. Hannewald, Phys. Rev. B **79**, 235206 (2009).

[21] F. Ortmann, F. Bechstedt, and K. Hannewald, J. Phys.: Condens. Matter **22**, 465802 (2010).

[22] A. Troisi and G. Orlandi, J. Phys. Chem. A **110**, 4065 (2006).

[23] N. Vukmirović, C. Bruder, and V. M. Stojanović, Phys. Rev. Lett. **109**, 126407 (2012).

[24] S. Fratini and S. Ciuchi, Phys. Rev. Lett. **103**, 266601 (2009).

[25] S. Fratini, S. Ciuchi, D. Mayou, G. T. de Laissardière, and A. Troisi, Nat. Mater. **16**, 998 (2017).

[26] A. Troisi, Phys. Rev. B **82**, 245202 (2010).

[27] S. Fratini, D. Mayou, and S. Ciuchi, Adv. Funct. Mater. **26**, 2292 (2016).

[28] S. Hutsch, M. Panhans, and F. Ortmann, Phys. Rev. B **104**, 054306 (2021).

[29] T. Nematiaram, D. Padula, A. Landi, and A. Troisi, Adv. Funct. Mater. **30**, 2001906 (2020).

[30] J. H. Fetherolf, D. Golež, and T. C. Berkelbach, Phys. Rev. X **10**, 021062 (2020).

[31] S. Giannini, A. Carof, M. Ellis, H. Yang, O. G. Ziogos, S. Ghosh, and J. Blumberger, Nat. Commun. **10**, 3843 (2019).

[32] A. Carof, S. Giannini, and J. Blumberger, Phys. Chem. Chem. Phys. **21**, 26368 (2019).

[33] G. Czycholl, *Theoretische Festkörperphysik - Von den klassischen Modellen zu modernen Forschungsthemen* (Springer-Verlag, Berlin, 2007).

[34] R. S. Sánchez-Carrera, P. Paramonov, G. M. Day, V. Coropceanu, and J.-L. Brédas, J. Am. Chem. Soc. **132**, 14437 (2010).

[35] A. Girlando, L. Grisanti, M. Masino, I. Bilotti, A. Brillante, R. G. Della Valle, and E. Venuti, Phys. Rev. B **82**, 035208 (2010).

[36] A. Girlando, L. Grisanti, M. Masino, A. Brillante, R. G. Della Valle, and E. Venuti, J. Phys. Chem. C **135**, 084701 (2011).

[37] V. Coropceanu, R. S. Sánchez-Carrera, P. Paramonov, G. M. Day, and J.-L. Brédas, J. Phys. Chem. C **113**, 4679 (2009).

[38] Y. Yi, V. Coropceanu, and J.-L. Brédas, J. Phys. Chem. C **137**, 164303 (2012).

[39] Y. Li, Y. Yi, V. Coropceanu, and J.-L. Brédas, Phys. Rev. B **85**, 245201 (2012).

[40] Z. Tu, Y. Yi, V. Coropceanu, and J.-L. Brédas, J. Phys. Chem. C **122**, 44 (2018).

[41] T. Nematiaram, S. Ciuchi, X. Xie, S. Fratini, and A. Troisi, J. Phys. Chem. C **123**, 6989 (2019).

[42] M. Panhans, S. Hutsch, J. Benduhn, K. S. Schellhammer, V. C. Nikolis, T. Vangerven, K. Vandewal, and F. Ortmann, Nat. Commun. **11**, 1488 (2020).

[43] See Supplemental Material at http://link.aps.org/supplemental/10.1103/PhysRevB.105.165136 for details of the derivation of vibrational disorder, which includes Refs. [79–81].

[44] I. G. Lang and Y. A. Firsov, Sov. Phys. JETP **16**, 1301 (1963).

[45] F. Ortmann and S. Roche, Phys. Rev. B **84**, 180302(R) (2011).

[46] R. Kubo, M. Yokota, and S. Nakajima, J. Phys. Soc. Jpn. **12**, 1203 (1957).

[47] R. Kubo, J. Phys. Soc. Jpn. **12**, 570 (1957).

[48] M. Panhans and F. Ortmann, Phys. Rev. Lett. **127**, 016601 (2021).

[49] Z. Fan, J. H. Garcia, A. W. Cummings, J. E. Barrios-Vargas, M. Panhans, A. Harju, F. Ortmann, and S. Roche, Phys. Rep. **903**, 1 (2021).

[50] R. Haydock, V. Heine, and M. J. Kelly, J. Phys. C **8**, 2591 (1975).
[51] S. Roche and D. Mayou, Phys. Rev. Lett. **79**, 2518 (1997).
[52] A. Weiße, G. Wellein, A. Alvermann, and H. Fehske, Rev. Mod. Phys. **78**, 275 (2006).
[53] F. Ortmann and S. Roche, Phys. Rev. Lett. **110**, 086602 (2013).
[54] D. Mayou, Phys. Rev. Lett. **85**, 1290 (2000).
[55] C. R. Groom, I. J. Bruno, M. P. Lightfoot, and S. C. Ward, Acta Crystallogr. B **72**, 171 (2016).
[56] H. C. Alt and J. Kalus, Acta Crystallogr. B **38**, 2595 (1982).
[57] T. Kubar, P. B. Woiczikowski, G. Cuniberti, and M. Elstner, J. Phys. Chem. B **112**, 7937 (2008).
[58] E. F. Valeev, V. Coropceanu, D. A. da Silva Filho, S. Salman, and J.-L. Brédas, J. Am. Chem. Soc. **128**, 9882 (2006).
[59] J. Blumberger, Chem. Rev. **115**, 11191 (2015).
[60] M. J. Frisch, G. W. Trucks, H. B. Schlegel, G. E. Scuseria, M. A. Robb, J. R. Cheeseman, G. Scalmani, V. Barone, G. A. Petersson, H. Nakatsuji *et al.*, Gaussian 16 Revision C.01 (Gaussian, Inc., Wallingford CT, 2016), https://gaussian.com/citation/.
[61] R. Krishnan, M. J. Frisch, and J. A. Pople, J. Chem. Phys. **72**, 4244 (1980).
[62] C. Lee, W. Yang, and R. G. Parr, Phys. Rev. B **37**, 785 (1988).
[63] A. D. Becke, J. Chem. Phys. **98**, 5648 (1993).
[64] P. E. Blöchl, Phys. Rev. B **50**, 17953 (1994).
[65] G. Kresse and D. Joubert, Phys. Rev. B **59**, 1758 (1999).
[66] G. Kresse and J. Hafner, Phys. Rev. B **47**, 558 (1993).
[67] G. Kresse and J. Furthmüller, Comput. Mater. Sci. **6**, 15 (1996).
[68] Y. C. Cheng, R. J. Silbey, D. A. Da Silva Filho, J. P. Calbert, J. Cornil, and J. L. Brédas, J. Chem. Phys. **118**, 3764 (2003).
[69] F. Giustino, Rev. Mod. Phys. **89**, 015003 (2017).
[70] B. Aradi, B. Hourahine, and T. Frauenheim, J. Phys. Chem. A **111**, 5678 (2007).
[71] M. Elstner and G. Seifert, Philos. Trans. R. Soc. A **372**, 20120483 (2014).
[72] X. Xie, A. Santana-Bonilla, and A. Troisi, J. Chem. Theory Comput. **14**, 3752 (2018).
[73] B. Hourahine, B. Aradi, V. Blum, F. Bonafé, A. Buccheri, C. Camacho, C. Cevallos, M. Y. Deshaye, T. Dumitrică, A. Dominguez *et al.*, J. Chem. Phys. **152**, 124101 (2020).
[74] M. Gaus, A. Goez, and M. Elstner, J. Chem. Theory Comput. **9**, 338 (2013).
[75] M. Gaus, X. Lu, M. Elstner, and Q. Cui, J. Chem. Theory Comput. **10**, 1518 (2014).
[76] Y. Yang, H. Yu, D. York, Q. Cui, and M. Elstner, J. Phys. Chem. A **111**, 10861 (2007).
[77] S. Grimme, J. Antony, S. Ehrlich, and H. Krieg, J. Chem. Phys. **132**, 154104 (2010).
[78] W. Warta and N. Karl, Phys. Rev. B **32**, 1172 (1985).
[79] L. Isserlis, Biometrika **12**, 134 (1918).
[80] G. C. Wick, Phys. Rev. **80**, 268 (1950).
[81] P. Danielewicz, Ann. Phys. **152**, 239 (1984).